Systematic study of ionic conduction in silver iodide / mesoporous alumina composites 1: Effects of pore size and filling level

Journal:	*Physical Chemistry Chemical Physics*
Manuscript ID	CP-ART-07-2023-003546.R1
Article Type:	Paper
Date Submitted by the Author:	08-Sep-2023
Complete List of Authors:	Fukui, Yoko; NBC Meshtec Inc Yoshida, Yukihiro; Kyoto Daigaku, Graduate School of Science Kitagawa, Hiroshi; Kyoto Daigaku, Graduate School of Science Jikihara, Yohei; NBC Meshtec Inc

PCCP

PAPER

Systematic study of ionic conduction in silver iodide / mesoporous alumina composites 1: Effects of pore size and filling level†

Yoko Fukui,*[a] Yukihiro Yoshida,*[b] Hiroshi Kitagawa[b] and Yohei Jikihara[a]

Received 00th January 20xx,
Accepted 00th January 20xx

DOI: 10.1039/x0xx00000x

A systematic study of Ag$^+$-ion conducting behavior in Ag$^+$-loaded porous materials was conducted over the entire sub-10 nm region for the first time. The effects of the pore diameter of mesoporous aluminas (MPAs) and the amount of silver iodide (AgI) loaded into MPAs were investigated using N$_2$ gas adsorption/desorption, powder X-ray diffraction, differential scanning calorimetry, and electrochemical impedance spectroscopy measurements. Confinement of AgI in the mesoporous space lowers the phase transition temperature between the β/γ- and α-phases relative to that of bulk AgI. The AgI-loading into the MPAs with smaller pores led to a more significant decrease in the transition temperature, possibly because the smaller AgI nanoparticles in the pores must have a higher surface energy to stabilize the high-temperature phase. The room-temperature ionic conductivity exhibits a volcano-type dependence on the pore diameter with the highest value when AgI was loaded into MPA with a pore diameter of 7.1 nm (7.2×10^{-4} S cm^{-1} at room temperature). Concerning the 7.1 nm-MPA, the room-temperature ionic conductivity was the highest for the nearly fully occupied composite, which is more than three orders of magnitude higher than that of the bulk AgI. The present study reveals that the Ag$^+$-ion conductivity in AgI/MPA composites can be controlled by optimizing the pore diameter of MPA and the AgI-loading ratio.

Introduction

Solid-state ionic conductors have been increasingly utilized in various applications such as batteries, fuel cells, sensors, electrochromic displays, catalysts, oxygen pumps, and so on.[1–7] Among them, silver iodide (AgI) is known to undergo a structural phase transition from the low-temperature β/γ-phase to superionic α-phase at 147 °C, which exhibits extraordinarily high ionic conductivity of the order of 1 S cm^{-1}, primarily because of melting on the cation sublattic.[8–12] Thus far, several attempts have been made to stabilize the α-phase at room temperature; for example, supercooling the AgI–Ag$_2$O–B$_2$O$_3$ glass matrix[13] and reducing the size of the AgI particles on the nanometer scale.[14–17] In the latter, AgI nanoparticles with a diameter of 6.3 nm stabilized the α-phase down to 37 °C. Whereas the high diffusivity of Ag$^+$ ions is largely attributed to the high fraction of Ag$^+$-ion vacant sites in α-AgI, the higher covalent bonding character of Ag–I compared to that of other silver halides could also modify the behavior in the favorable direction of increased Ag$^+$ diffusivity. Therefore, it is most likely that the introduction of Ag$^+$-ion vacant sites, even if not in the α-phase, is promising for providing highly ion-conducting AgI.

The space-charge layer formed at a heterogeneous interface facilitates the migration of ions, impurities, or point defects, which is the main factor for the increased ionic conductivity in heterogeneously doped solid electrolytes.[18–23] Although the first report by Liang in 1973 demonstrated that the dispersion of insulating alumina particles in the LiI matrix led to the increase in the ionic conductivity by more than an order of magnitude,[24] incorporation of AgI into porous insulators such as alumina,[25–36] silica,[37–43] zeolite,[44] and zirconia[37] has provided a unique subclass of highly ion-conducting composites. Such composites are promising for use as the solvent-free electrolytes in electrochemical devices because of their infinite conducting pathway for Ag$^+$ ions, in contrast to AgI nanoparticles embedded with organic polymers (i.e., polyvinylpyrrolidone).[14–17] Furthermore, it is known that the formation of Frenkel defects, comprising interstitial Ag$^+$ ions and Ag$^+$-ion vacant sites, near the surface of the particles is responsible for the enhanced Ag$^+$-ion conductivity observed for AgI nanoparticles.[18] Although it is difficult to assess the Debye length characterizing the dimension of the space-charge layer, AgI particles introduced into the nanometer-scale pores have a significant surface energy, which efficiently produces mobile Ag$^+$ ions. Despite the fact that the porous structure (pore size and topology) of the porous matrix and the filling level of AgI inevitably affect the ion-conducting properties of the composites, systematic variations, especially on the pore size in the sub-10 nm region, to achieve rational control of the Ag$^+$-ion conductivity have not yet been investigated. In this study, we investigate the structural, thermal, and ion-conducting properties of AgI-loaded mesoporous aluminas (MPAs) with different pore sizes (peak pore diameter: 2.4–15.9 nm) with different AgI-loading levels, for the purpose of the application as solvent-free electrolytes in electrochemical

---

[a] NBC Meshtec Inc., 2-50-3 Toyoda, Hino, Tokyo 191-0053, Japan. E-mail: fukui.yoko@nisshin.com

[b] Division of Chemistry, Graduate School of Science, Kyoto University, Kitashirakawa-Oiwakecho, Sakyo-ku, Kyoto 606-8502, Japan. E-mail: yoshiday@ssc.kuchem.kyoto-u.ac.jp

† Electronic Supplementary Information (ESI) available: Figs. S1–S13. See DOI: 10.1039/x0xx00000x

devices. This paper presents the pore-size dependence of the thermal and ion-conducting properties of AgI/MPA composites formed with six types of MPAs (denoted as MPA1 – MPA6; Table 1), along with the AgI-loading ratio dependence for AgI/MPA3 with the highest ionic conductivity among the six AgI/MPA composites.

Experimental section

Materials. In this study, we used six types of commercially available MPAs; namely, MPA1: Versal V-GL15 (Union Showa Co., Ltd.), MPA2: Versal V-250 (Union Showa Co., Ltd.), MPA3: Aluminum oxide, mesoporous 517747 (Sigma-Aldrich Japan), MPA4: Aluminum oxide 199443 (Sigma-Aldrich Japan), MPA5: Activated alumina A11 (Sumitomo Chemical Co., Ltd.), and MPA6: Versal V-R-3 (Union Showa Co., Ltd.). Prior to use, the MPAs and AgI (Kojima Chemicals Co., Ltd., 99.0%, Japan) were dried at 500 and 200 °C, respectively, for 6 h under N_2 atmosphere. Adequate amounts of dried MPA and AgI, namely, volumetric loading fractions of AgI of ca. 90 vol% for the pore-size dependent experiments and 7–241 vol% (volumetric loading ratio: 1:9–8:2 for AgI/MPA3) for the loading ratio dependent experiments, were co-ground in an agate mortar under low humidity (volumetric moisture content: < 0.35%) in a N_2-filled glovebox. Each mixed powder of AgI/MPA was pressed at 500 MPa for 1 min to obtain a compressed pellet with a diameter of 2.5 mm, followed by heat treatment at 600 °C for 20 h to introduce AgI (melting point: 552 °C) into the MPA pores.

Characterization. N_2 gas sorption isotherms were measured at 77 K with a BELSORP-miniII volumetric adsorption system, whereas water vapor sorption isotherms were measure at 298 K with a BELSORP-max volumetric adsorption system. Scanning electron microscope (SEM) observation and energy dispersive X-ray spectroscopy (EDS) analysis were performed with a JSM-IT500HR at an accelerating voltage of 15 kV for SEM and 20 kV for EDS. Room-temperature powder X-ray diffraction (PXRD) measurements were performed with a Bruker D8 ADVANCE instrument using Cu Kα radiation (λ = 1.5418 Å). Variable-temperature PXRD measurements were performed using a synchrotron X-ray (λ = 0.699585(1) Å) at the BL02B2 beamline in SPring-8 on a Dectris MYTHEN detector. The temperature was controlled using a stream of nitrogen gas at a rate of 50 K min^{-1}. Rietveld refinements to evaluate the ratio of α-AgI phase were performed with fixed atomic coordinates. The thermal properties were characterized by differential scanning calorimetry (DSC) thermograms using a NETZSCH DSC 3500 Sirius instrument equipped with N_2 cryostatic cooling. The composites, which were sealed in aluminum pans, were heated from room temperature to 200 °C, followed by cooling to 0 °C at a heating and cooling rate of 5 °C min^{-1}. The ionic conductivities of the pellets were measured by the AC impedance technique with an applied voltage of 100 mV using a Solartron SI 1260 Impedance/Gain-phase Analyzer and 1260A Dielectric Interface in the frequency range of 1 MHz to 0.1 Hz. Both sides of the pellets were painted with gold paste (Tokuriki, 8560-1A) and measurements were performed in a temperature- and humidity-controlled chamber ESPEC SH-221 or a temperature-controlled chamber ESPEC ST-110. The impedance was determined from the first real axis touchdown point in the Nyquist plot.

Table 1. Mesoporous aluminas (MPAs) used in this study

Notation	Structure[a]	Pore diameter[b] (nm)	Pore volume[b] (cm^3 g^{-1})	Specific surface area[b] (m^2 g^{-1})
MPA1	γ and δ	15.9	0.895	149.8
MPA2	γ	9.2	1.005	318.3
MPA3	γ	7.1	0.455	241.4
MPA4	γ	5.5	0.268	139.0
MPA5	γ and χ	5.5	0.247	120.7
MPA6	χ	2.4	0.203	240.6

[a] After heat treatment (Fig. S1, ESI†).[45] [b] Estimation based on N_2 gas sorption measurements after heat treatment (Figs. 1 and S2 (ESI†)).

Results and Discussion

Fig. 1 shows the pore size distributions of six types of heat-treated MPAs used in this study, where the Barrett–Joyner–Halenda (BJH) method[46] was applied to the measured N_2 gas adsorption isotherms (Fig. S2, ESI†). The pore diameter is defined herein as the point at which the differential pore volume exhibited a maximum value. As shown in Table 1, the pore diameter, pore volume, and specific surface area lie within the range of 2.4–15.9 nm, 0.203–1.005 cm^3 g^{-1}, and 120.7–318.3 m^2 g^{-1}, respectively. Using these MPAs, we investigated the pore size dependence of the structural, thermal, and ion-conducting properties of the AgI-loaded MPAs.

Pore-size dependence. To the best of our knowledge, there are three studies examining the relationship between the ionic conductivity and pore size in AgI-loaded mesoporous materials; namely, AgI-loaded mesoporous silica (MPS) with a pore diameter of 2.0–5.2 nm (6 kinds of composites),[39,40] AgI-loaded MPS with a pore diameter of 4–40 nm (3 kinds of composites),[38]

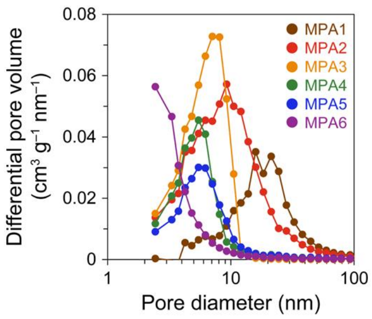

Fig. 1 Pore size distribution of heat-treated MPAs (brown: MPA1, red: MPA2, orange: MPA3, green: MPA4, blue: MPA5, purple: MPA6) obtained by applying the BJH method to the measured N_2 adsorption isotherms (Fig. S2, ESI†).

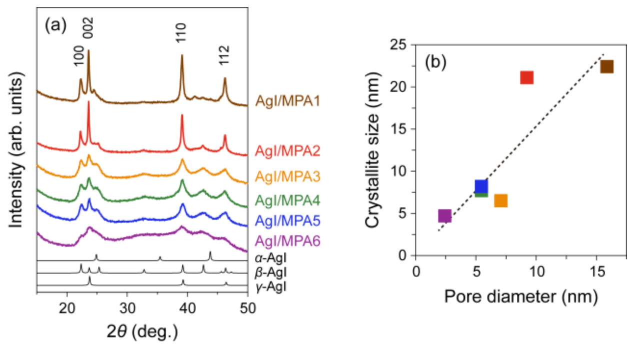

Fig. 2 (a) PXRD patterns of AgI/MPA composites (brown: AgI/MPA1, red: AgI/MPA2, orange: AgI/MPA3, green: AgI/MPA4, blue: AgI/MPA5, purple: AgI/MPA6) along with simulated patterns (black thin lines) of *α*-, *β*-, and *γ*-AgI (from the top). (b) Correlation between the crystallite size of *β*-AgI phase and pore diameter of MPAs in AgI/MPA composites.

and AgI/Ag-loaded anodic alumina with a pore diameter of 10–20 nm (3 kinds of composites).[34] Notably, the last example demonstrated that the room-temperature ionic conductivity of AgI/Ag heteronanowires embedded in an anodic alumina membrane increases as the pore size decreases, and the smallest pore (i.e., 10 nm) leads to the highest Ag$^+$-ion conductivity. In addition, Maekawa *et al.* reported that LiI/MPA (ion size; Li$^+$: 0.090 nm vs. Ag$^+$: 0.129 nm[47]) composites exhibited the highest Li$^+$-ion conductivity when using MPAs with pore diameters of 4–7 nm.[48,49] These findings motivated us to explore the optimal pore size for highly Ag$^+$-ion conducting AgI/MPA composites at the sub-10 nm scale. To this end, we chose six kinds of commercially available MPAs with pore diameters in the range of 2.4–15.9 nm, as listed in Table 1. Each MPA was co-ground with AgI at an appropriate loading ratio such that the volumetric loading fraction of AgI in the pores of the MPAs is approximately 90% followed by heat treatment at 600 °C for 20 h. SEM images confirmed that the surface morphology of MPA remains intact during the heat treatment (Fig. S3, ESI†). N_2 gas sorption analysis of the AgI/MPA composites (Fig. S4, ESI†) revealed that the pore space of the MPAs was nearly fully occupied by AgI, which was consistent with the homogeneous elemental distribution of Ag, Al, I, and O in the EDS mapping (Fig. S5, ESI†). All the peaks observed in the PXRD patterns of the AgI/MPA composites can be assigned to the *β*- or *γ*-phase with different peak widths (Fig. 2a). The difference was more marked when the crystallite size of the *β*-AgI phase, estimated based on the Le Bail method,[50] was plotted against the pore diameter of the MPAs (Fig. 2b). This clear positive correlation is considered evidence of the incorporation of AgI into the pores of the MPAs.

To investigate the effect of the pore size on the thermal behavior, the DSC profiles of the AgI/MPA composites were measured during the heating and cooling processes. Focusing on the cooling process, a sharp exothermic peak derived from the *α*- to *β*/*γ*- phase transition was observed at 143 °C for the parent bulk AgI (Fig. 3a; red arrow), whereas two peaks were observed for the composites with the MPAs having a larger pore diameter (i.e., MPA1, MPA2, and MPA3). The AgI/MPA1 and AgI/MPA2 composites showed a more pronounced peak on the high-temperature side (Figs. 3b and 3c; red arrow), whereas the AgI/MPA3 composite on the low-temperature side (Fig. 3d; blue arrow). As is evident in the following section, all AgI particles were loaded into the pores in the AgI/MPA composites with a volumetric loading fraction of AgI of approximately 90%, thereby indicating that both peaks can be assigned to the phase

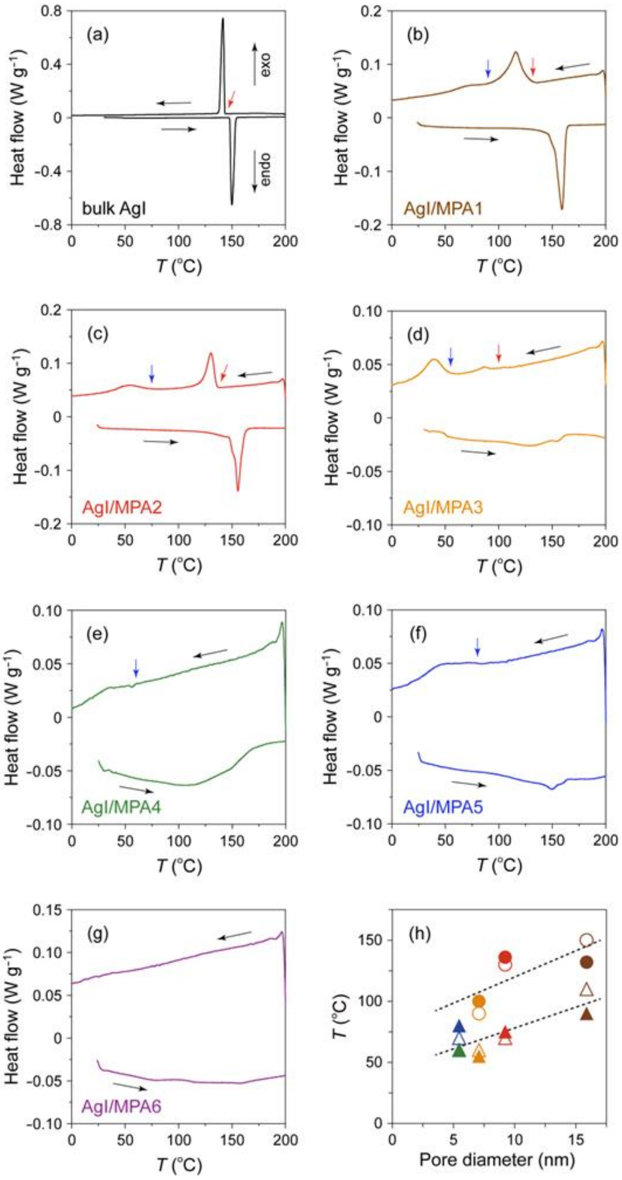

Fig. 3 DSC profiles of AgI/MPA composites ((a) bulk AgI, (b) AgI/MPA1, (c) AgI/MPA2, (d) AgI/MPA3, (e) AgI/MPA4, (f) AgI/MPA5, and (g) AgI/MPA6). The red and blue arrows indicate the onset temperatures of the transition on the high and low temperature sides, respectively, in the cooling process. (h) Pore diameter dependence of the transition temperatures determined by DSC (closed circles: high-temperature peak, closed triangles: low-temperature peak) and the temperatures at which the temperature differential of *σ* shows a maximum (open circles: high-temperature peak, open triangles: low-temperature peak) in the cooling process.

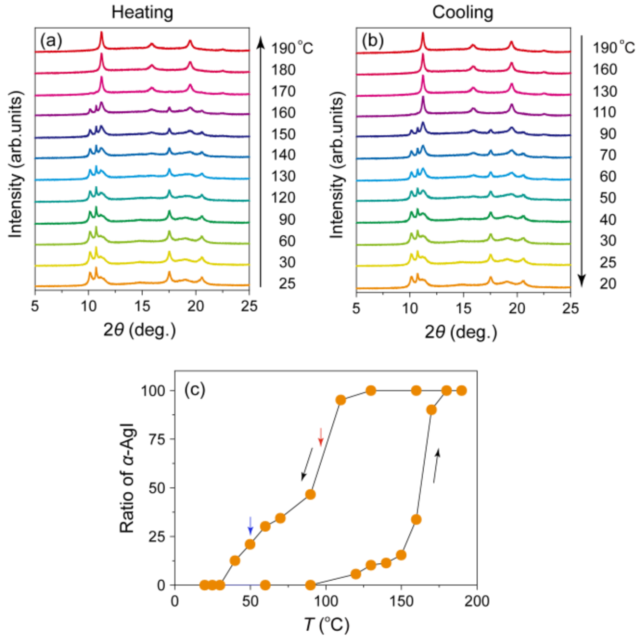

Fig. 4 Variable-temperature synchrotron PXRD patterns of AgI/MPA3 composite in the heating (a) and cooling (b) processes (λ = 0.699585(1) Å). (c) Temperature dependence of the ratio of α-AgI phase determined by the Rietveld method, where the red and blue arrows indicate the temperatures at which the temperature differential of the α-phase ratio shows a maximum.

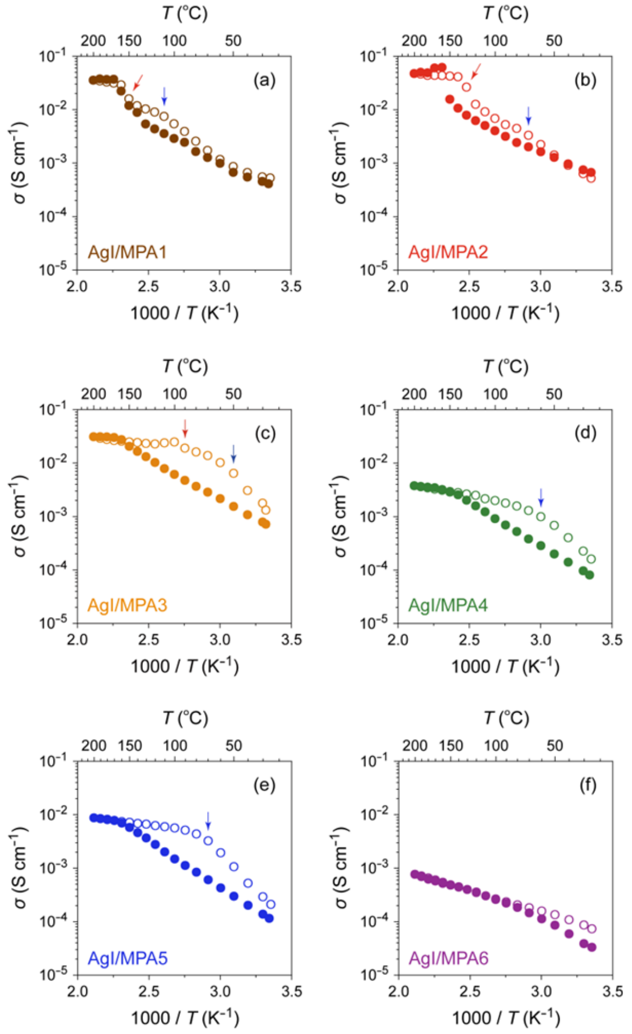

Fig. 5 Temperature dependence of σ for AgI/MPA composites ((a) AgI/MPA1, (b) AgI/MPA2, (c) AgI/MPA3, (d) AgI/MPA4, (e) AgI/MPA5, and (f) AgI/MPA6) in heating (closed circles) and cooling (open circles) processes. The red and blue arrows indicate the temperatures at which the temperature differential of σ shows a maximum.

transition of AgI loaded into the pores. The DSC profiles of the AgI/MPA3 composites obtained by heat treatment at 400, 500, and 600 °C, which spans the melting point of AgI (552 °C; Fig. S6, ESI†), support the assignment. Only an exothermic peak, possibly corresponding to that on the low temperature side, was observed for the composites of the MPAs with a smaller pore diameter (i.e., MPA4 and MPA5; Figs. 3e and 3f), whereas the peak was hardly visible for the AgI/MPA6 composite of MPA6 with the smallest pore diameter (Fig. 3g) as in AgI nanoparticles with a diameter of ca. 3.0 nm.[17] To date, the origin of the multiple DSC peaks of the AgI-based composites is still under debate and several origins such as inhomogeneous incorporation,[51] mechanical stress,[52] and the 7H-AgI phase (7-layered structure with the stacking sequence of ABCBCAC)[51,53–55] have been proposed. However, given that the onset temperatures of both the high- and low-temperature peaks decrease with decreasing pore diameter of the MPAs as shown in Fig. 3h, the thermal behavior can best be thought of as a manifestation of the nano-sized effect, which stabilizes the high-temperature phase owing to the increased surface energy of the small particles. A similar trend was previously reported for AgI nanoparticles.[14–17] Accordingly, the thermal properties of AgI can be controlled through the rational selection of mesoporous materials, without using protective polymers that disturb long-range migration of the Ag^+ ions.

Variable-temperature PXRD measurements of the AgI/MPA3 composite also confirmed the phase transition to α-AgI in the composites. All the PXRD peaks observed at 25 °C, which are assigned to either β- or γ-AgI, rapidly disappeared with the concurrent appearance of new peaks at 2θ = 11.2, 15.9, 19.5, and 22.5 ° in the temperature range of 150–170 °C (Fig. 4a). The α-phase is reversibly transformed to the β/γ-phase at 90–110 °C in the subsequent cooling process (Fig. 4b); namely, the transition can be regarded as a first-order transition because of the observed thermal hysteresis. Notably, the room-temperature PXRD pattern after cyclic heating and cooling treatments showed no trace of 7H-AgI peaks, as observed previously.[51,53–55] The phase transition was more explicit when the α-AgI ratio was plotted as a function of temperature, which was determined by the Rietveld method (Figs. 4c and S7 (ESI†)). The α-AgI ratio gradually decreased to 30 °C after the rapid decrease at 90–110 °C in the cooling process. The temperatures, at which the α-AgI ratio shows a pronounced decrease (i.e., ca. 100 °C and ca. 50 °C as indicated by red and blue arrows, respectively), are consistent with the exothermic peaks observed in the DSC profile (Fig. 3d).

The ionic conductivity (σ) of the AgI/MPA composites with different pore diameters was measured using AC impedance spectroscopy. The room-temperature ionic conductivities ($\sigma_{25°C}$) were estimated to be 4.1 × 10^{-4}, 6.8 × 10^{-4}, 7.2 × 10^{-4}, 8.1 × 10^{-5}, 1.2 × 10^{-4}, and 3.3 × 10^{-5} S cm^{-1} for AgI/MPA1–AgI/MPA6, respectively. All the AgI/MPA composites have a higher $\sigma_{25°C}$ value than that of bulk AgI (ca. 1.5 × 10^{-7} S cm^{-1}),[14] as reported previously.[25–36] It is apparent that the formations of the space-charge layer at the interface between AgI and MPA and the Frenkel defects near the surface of the AgI particles could have a favorable effect on the Ag^+ migration.[18–23] We note that the $\sigma_{25°C}$ value of AgI/MPA3 before heat treatment (4.6 × 10^{-5} S cm^{-1}; Fig. S8, ESI†) is more than an order of magnitude lower than that of heat-treated AgI/MPA3 (7.2 × 10^{-4} S cm^{-1}). Upon heating, all composites followed the Arrhenius law given by the equation, $\sigma T = A\ \exp(-E_a/k_BT)$, where A is the pre-exponential factor, E_a is the activation energy, and k_B is the Boltzmann constant, up to approximately 100 °C (Fig. 5). The E_a values were estimated in the range of 0.25–0.36 eV; however, there was no simple correlation with the pore diameter. Above this temperature, the composites of AgI/MPA1 and AgI/MPA2 with a larger pore diameter showed a discontinuous change at ca. 150 °C, which is reminiscent of the phase transition from the low-temperature β/γ-phase to superionic α-phase in bulk AgI.[8–12] These composites showed a sharp endothermic DSC peak at aforementioned temperatures, and therefore, it is possible that the bulk-like AgI occupying the core of the mesopores is responsible for the phase transition. In the case of AgI/MPA3–AgI/MPA6 with a smaller pore diameter, the slope showed a continuous variation (E_a = 0.09–0.21 eV at 170–200 °C) because of the nano-sized effect. As reported previously,[13,14,16,29,32,34,35,37,42,43,51,53–55] the ion-conducting behavior in the cooling process was different from that in the heating process for each composite, where the room-temperature PXRD pattern remained unchanged after the cyclic heating and cooling processes (Fig. S9, ESI†). Notably, the temperatures at which the temperature differential of σ exhibits a maximum (red and blue arrows in Figs. 5a–e) are comparable to the onset temperatures of the exothermic DSC peaks observed during the cooling process (Fig. 3h). Accordingly, it is apparent that the observed peculiar behavior of σ is closely connected to the structural transitions from the superionic α-AgI phase to the thermally stable β/γ-AgI phases. The thermal hysteresis observed in DSC and ionic conductivity measurements is associated with the suppression of the phase transition of AgI during both heating and cooling processes, possibly as a consequence of the inhomogeneous charge distribution of AgI particles near the surface of the MPAs.[14,34,37]

Fig. 6 shows the pore size dependence of $\sigma_{25°C}$ and the molar conductivity ($\Lambda_{25°C} = \sigma_{25°C}$ / [molar concentration of loaded AgI]) for the AgI/MPA composites with different pore diameters. Notably, the Λ value is originally proportional to the ion diffusivity (D) at a certain temperature according to the Nernst–Einstein equation, $D = RT\Lambda/z^2F^2$, where R is the universal gas constant, z is the charge of the ions, and F is the Faraday constant. Both kinds of conductivity show a volcano-type dependence with a maximum at 7.1 nm (i.e., AgI/MPA3) for $\sigma_{25°C}$ and 9.2 nm (i.e., AgI/MPA2) for $\Lambda_{25°C}$. Similar behavior has been reported for LiI/MPA composites, where the highest Li^+-ion conductivity was observed for the composites with the pore diameter of 4–7 nm.[48,49] Although the magnitude of the Debye length remains a matter of debate,[18,56] it is possible that the decreased conductivities in the composites with a large pore diameter (i.e., AgI/MPA1) are associated with the decreased fraction of "surface" ions that efficiently produce Frenkel defects including mobile Ag^+ ions; namely, bulk-like AgI occupying the core of the mesopores contributes largely to ion-conducting behavior in these composites as described above. This trend is the same as AgI/AAO (AAO: anodic aluminum oxide), in which the room-temperature σ value decreases as the pore diameter increases from 10 to 20 nm.[34] The decreased conductivities of the composites with small pore diameters (i.e., AgI/MPA4, AgI/MPA5, and AgI/MPA6) may be attributed to the confinement of Ag^+ ions near the pore surfaces of the MPAs, leading to the formation of an electric double layer. In other words, the Coulomb interactions between the Ag^+ ions and nucleophilic O^{2-} ions on the surface of the MPAs may suppress the migration of the Ag^+ ions. To the best of our knowledge, the room-temperature ionic conductivity in AgI-loaded composites with porous silica is 1.2 × 10^{-4} S cm^{-1} at the highest.[37] Because the value is significantly lower than that of many AgI-loaded composites with porous alumina[25–36] including the present composites, it is evident that the present results provide

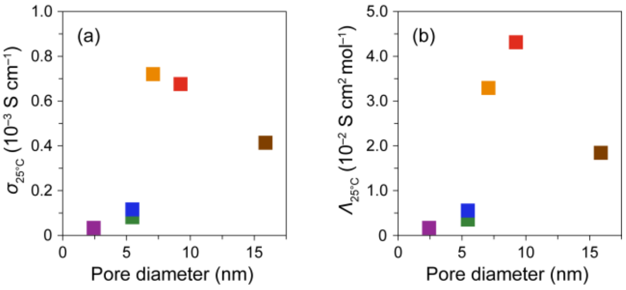

Fig. 6 Plots of (a) $\sigma_{25°C}$ and (b) $\Lambda_{25°C}$ against pore diameter of MPA (brown: AgI/MPA1, red: AgI/MPA2, orange: AgI/MPA3, green: AgI/MPA4, blue: AgI/MPA5, purple: AgI/MPA6).

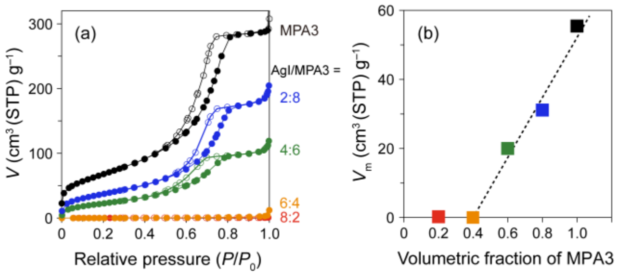

Fig. 7 (a) N_2 gas adsorption (closed circles) and desorption (open circles) isotherms of AgI/MPA3 composites with different volumetric loading levels at 77 K (red: AgI/MPA3 = 8:2, orange: AgI/MPA3 = 6:4, green: AgI/MPA3 = 4:6, blue: AgI/MPA3 = 2:8, black: parent MPA3). (b) Loading ratio dependence of monolayer adsorption amount (V_m) of AgI/MPA3 composites.

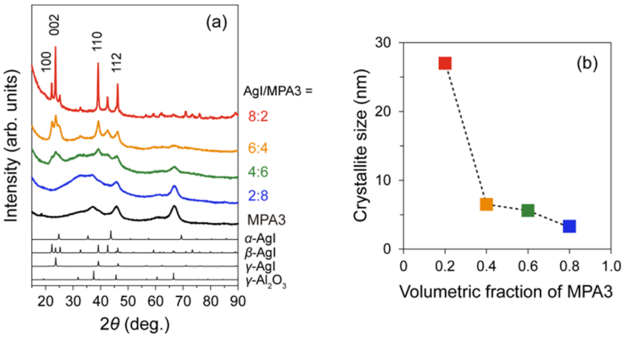

Fig. 8 (a) PXRD patterns of AgI/MPA3 composites (red: AgI/MPA3 = 8:2, orange: AgI/MPA3 = 6:4, green: AgI/MPA3 = 4:6, blue: AgI/MPA3 = 2:8, black: parent MPA3) along with simulated patterns (black thin lines) of *α*-, *β*-, and *γ*-AgI and *γ*-Al_2O_3 (from the top). (b) Loading ratio dependence of crystallite size of *β*-AgI phase in AgI/MPA3 composites estimated using the Le Bail method.

important insights toward more judicious selection of porous alumina for highly Ag^+-ion conducting composites.

Loading ratio dependence. We investigated the effect of the AgI-loading ratio on the thermal and ion-conducting properties of AgI/MPA3, which exhibited the highest ionic conductivity among the composites prepared in this study. The N_2 isotherm of the parent MPA3 is categorized as typical type IV in the IUPAC nomenclature (Figs. 7a and S2 (ESI†));[57] namely, there is a pronounced uptake at approximately P/P_0 = 0.7 as a manifestation of the presence of mesopores. The N_2 uptake decreased steadily with increasing AgI-loading ratio and eventually became negligible for the composites with volumetric loading ratios higher than AgI/MPA3 ≥ 6:4 (Fig. 7b). This trend provides firm evidence of the incorporation of AgI into the mesopores of MPA3, where an excess of AgI was loaded into the composite with AgI/MPA3 = 8:2. The volumetric loading fraction of AgI in the pores of MPA3 with an upper loading ratio limit of AgI/MPA3 = 6:4 was estimated to be ca. 90 vol% (the same as AgI/MPA3 in the previous section) based on a comparison of the maximum N_2 uptake capacity with that of the parent MPA3.

Given that the PXRD peaks assigned to *β*- or *γ*-AgI became broader for the AgI/MPA3 = 6:4 composites when the loading temperature was increased from 400 to 600 °C (Fig. S10, ESI†), the broadened PXRD peaks observed for the composites with AgI/MPA3 < 8:2 (Fig. 8) apparently arose from the reduced size of AgI crystallite as a consequence of the incorporation into the mesopores of MPA3 as evidenced by the sorption measurements. The crystallite size (6.5 nm) of the *β*-AgI phase in the AgI/MPA3 = 6:4 composite with fully occupied pores, as estimated from the Le Bail refinement of the PXRD pattern (Fig. S11, ESI†), was comparable to the pore diameter of MPA3 (7.1 nm). The sharpened peaks arising from the increased crystallite size in the AgI/MPA3 = 8:2 composite were apparently caused by the presence of bulk AgI, which could not be loaded into the pores but was deposited on the surface of the grains of MPA3.

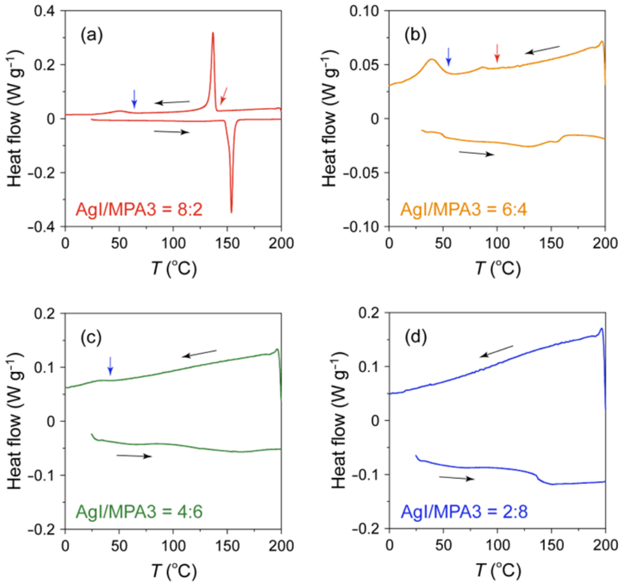

Fig. 9 DSC profiles of AgI/MPA3 composites ((a) AgI/MPA3 = 8:2, (b) AgI/MPA3 = 6:4 (same as Fig. 3d), (c) AgI/MPA3 = 4:6, and (d) AgI/MPA3 = 2:8). The red and blue arrows indicate the onset temperatures of the transitions on the high and low temperature sides, respectively, in the cooling process.

Fig. 9 shows the DSC profiles of the AgI/MPA3 composites with different loading ratios. During the cooling process, the AgI/MPA3 composites with high AgI-loading ratios exhibited two distinct peaks (Figs. 9a and 9b), as shown in Fig. 3d for the AgI/MPA3 = 6:4 composite. Only a low-temperature peak was observed for the AgI/MPA3 = 4:6 composite (Fig. 9c), whereas no distinct peak was observed for the AgI/MPA3 = 2:8 composite primarily because of the small amount of loaded AgI (Fig. 9d). Based on the dependence of the relative intensities on the AgI-loading ratio, it can be considered that the high- and low-temperature peaks are associated with bulk-like AgI occupying the core and AgI near the surface of the pores, respectively. The transition temperatures decreased with a decrease in the amount of loaded AgI as shown in Fig. 10f. Because the crystallite size of AgI steadily decreased as the amount of loaded AgI decreased as described above (Fig. 8b), the lowered transition temperatures can be qualitatively explained in terms of the increased surface energy of nano-sized AgI as described in the previous section.

Fig. 10a shows the dependence of $\sigma_{25^\circ C}$ and $\Lambda_{25^\circ C}$ on the AgI-loading ratio. Both conductivities show a volcano-type dependence on the loading ratio with a maximum for the AgI/MPA3 = 6:4 composite, where both conductivities ($\sigma_{25^\circ C}$ = 7.2×10^{-4} S cm^{-1} and $\Lambda_{25^\circ C}$ = 3.3×10^{-2} S cm^2 mol^{-1}) are more than three orders of magnitude higher than those of bulk AgI. The decreased conductivity under over-loading conditions (i.e., AgI/MPA3 = 8:2) apparently arose from bulk AgI with low $\sigma_{25^\circ C}$ (ca. 1.5×10^{-7} S cm^{-1} [14]) that could not be incorporated into the pores. In contrast, the gradual decrease in the conductivities of the AgI/MPA3 composites with lower AgI-loading ratios is attributable to the interruption of the percolation pathways of

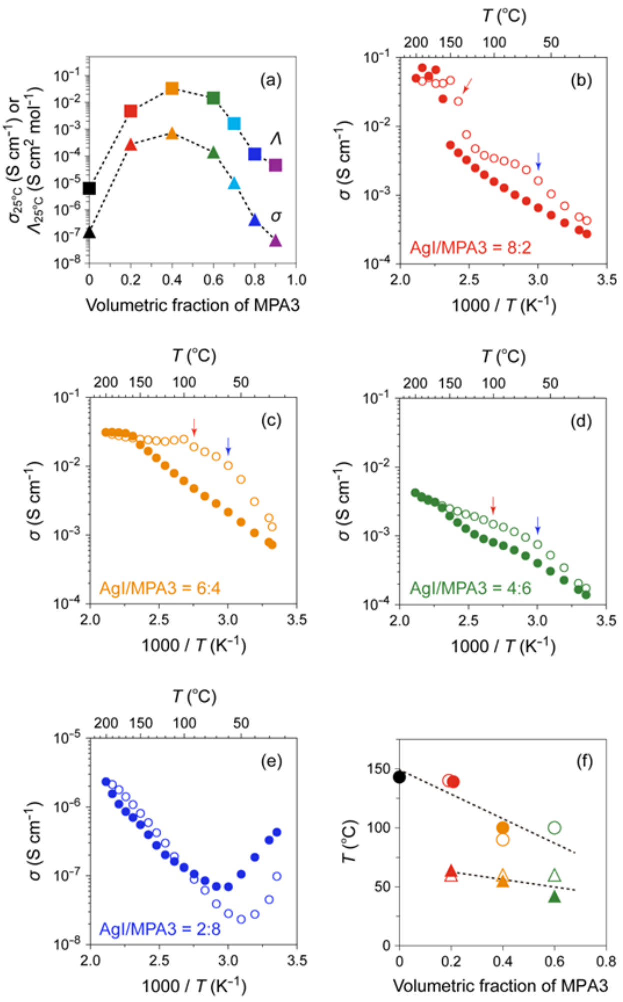

Fig. 10 (a) Loading ratio dependence of room-temperature ionic conductivity of AgI/MPA3 composites (black: AgI, red: AgI/MPA3 = 8:2, orange: AgI/MPA3 = 6:4, green: AgI/MPA3 = 4:6, blue: AgI/MPA3 = 2:8). Temperature dependence of ionic conductivity (*σ*) of AgI/MPA3 composites ((b) AgI/MPA3 = 8:2, (c) AgI/MPA3 = 6:4 (same as Fig. 5c), (d) AgI/MPA3 = 4:6, and (e) AgI/MPA3 = 2:8) in heating (closed circles) and cooling (open circles) processes. The red and blue arrows indicate the temperatures at which the temperature differential of *σ* shows a maximum. (f) Loading ratio dependence of the transition temperatures determined by DSC (closed circles: high-temperature peak, closed triangles: low-temperature peak) and the temperatures at which the temperature differential of *σ* shows a maximum (open circles: high-temperature peak, open triangles: low-temperature peak).

surface regions with mobile Ag$^+$ ions formed by the space-charge effect and Frenkel defects.[30,58,59]

Figs. 10b–e show the temperature dependence of *σ* for the AgI/MPA3 composites with different loading ratios. Upon heating, the *σ* value of all the composites, except for AgI/MPA3 = 2:8, showed Arrhenius-like behavior up to ca. 100 °C, where the E_a values lie in the range of 0.25–0.31 eV. The anti-Arrhenius behavior observed for the AgI/MPA3 = 2:8 composite below approximately 70 °C (Fig. 10e) is associated with the contribution of proton conduction driven by possible partial hydroxylation on the pore surface of MPA3 followed by proton migration through the water molecules occupying the pore.[60] Such behavior was also observed for other low AgI-loaded composites, AgI/MPA3 = 3:7 and 1:9 (Fig. S12, ESI†). To evaluate the contribution of the protons to the observed ionic conduction, the humidity-dependent ionic conductivity of the composites with AgI/MPA3 = 6:4 and 3:7 was measured at 25 °C. As shown in Fig. S13a (ESI†), the AgI/MPA3 = 6:4 composite exhibited nearly humidity-independent *σ* in the relative humidity (RH) range of 30–95%, indicating that Ag$^+$ migration is the dominant factor determining the ion conduction in the composite. On the other hand, the *σ* value varied greatly depending on the RH in the AgI/MPA3 = 3:7 composite with a rapid increase in *σ* at 70% RH ($\sigma_{25°C}$ = 1.0 × 10^{-5} S cm^{-1} at 30% RH and 6.6 × 10^{-5} S cm^{-1} at 95% RH; Fig. S13b, ESI†). Given that the amount of adsorbed water also increased sharply at P/P_0 = 0.7 for the AgI/MPA3 = 3:7 composite (Fig. S13d, ESI†), it is obvious that the *σ* value of the AgI/MPA3 = 3:7 composite is mainly derived from proton migration through the water molecules in the pores. For the AgI/MPA3 = 6:4 composite, the negligible water adsorption (Fig. S13c, ESI†) again confirmed that the proton contribution is of no significance for the ionic conduction. In the case of the over-loaded AgI/MPA3 = 8:2 composite, the *σ* value exhibited a significant discontinuous increase at ca. 150 °C in the heating process (Fig. 10b), at which the DSC profile exhibited a sharp endothermic peak (Fig. 9a). In the cooling process, the temperatures at which the temperature differential of *σ* exhibited a maximum was comparable to the onset temperatures of the exothermic DSC peaks observed during the cooling process (Fig. 10f), as in the previous section. The observed peculiar behavior of *σ* is thus closely connected with the structural transitions from the superionic *α*-AgI phase to the thermally stable *β*/*γ*-AgI phases. The decrease in the transition temperatures with decreasing AgI-loading ratio is closely related to the decreased size of the AgI particles in the pores as mentioned above.

Conclusions

In summary, by investigating the structural, thermal, and ion-conducting properties of AgI-loaded MPAs with various pore sizes and filling levels, we gained deeper insight into the relationship between the loading state of AgI and the ionic conduction of the AgI/MPA composites. In particular, the present study is the first to reveal that AgI-occupied mesopores with a moderate diameter (7.1 nm) show the highest Ag$^+$-ion conductivity at room temperature (7.2 × 10^{-4} S cm^{-1}), possibly because of the large fraction of the surface region that includes the mobile Ag$^+$ ions in the mesopores. The Ag$^+$-ion conductivity showed a pronounced thermal hysteresis associated with the structural transition between the low-conducting *β*/*γ*-phase and superionic *α*-phase. In contrast with the superionic AgI nanoparticles embedded in organic polymers, the AgI/MPA composites facilitate long-range Ag$^+$-ion migration, making them viable candidates for application in the field of solid-state ionics. It is inferred that the Ag$^+$-ion conduction in AgI-loaded composites depends greatly on the types of porous materials and loaded silver salts in addition to the pore size and filling level, as demonstrated in this study. Studies along this line, particularly on the effect of silver salt species, are in progress.

Conflicts of interest

There are no conflicts to declare.

Acknowledgements

This work was supported by the ACCEL program (JPMJAC1501) of the Japan Science and Technology Agency (JST) and JSPS KAKENHI Grant Numbers JP20H02708 and JP20H05623. Synchrotron PXRD measurements were conducted at beamline BL02B2 at SPring-8 with the approval of the Japan Synchrotron Radiation Research Institute (JASRI) (Proposal No. 2021A1296). The authors thank Drs. S. Kawaguchi and S. Kobayashi (JASRI) for their assistance with the experiments at SPring-8, and Prof. O. Kamishima (Setsunan University) for helpful discussions.

Notes and references

1 P. Knauth and J. Schoonman, *Nanostructured Materials: Selected Synthesis Methods, Properties and Applications*, Kluwer Academic Publishers, Dordrecht, 2002.
2 T. Minami, M. Tatsumisago, M. Wakihara, C. Iwakura, S. Kohjiya and I. Tanaka, *Solid State Ionics for Batteries*, Springer, Tokyo, 2005.
3 J. Schoonman, *Solid State Ionics*, 2000, **135**, 5–19.
4 P. Knauth and H. L. Tuller, *J. Am. Ceram. Soc.*, 2002, **85**, 1654–1680.
5 K. Funke, *Sci. Technol. Adv. Mater.*, 2013, **14**, 043502.
6 Z. Zou, Y. Li, Z. Lu, D. Wang, Y. Cui, B. Guo, Y. Li, X. Liang, J. Feng, H. Li, C. W. Nan, M. Armand, L. Chen, K. Xu and S. Shi, *Chem. Rev.*, 2020, **120**, 4169–4221.
7 F. Wu, L. Liu, S. Wang, J. Xu, P. Lu, W. Yan, J. Peng, D. Wu and H. Li, *Prog. Mater. Sci.*, 2022, **126**, 100921.
8 C. Tubandt and E. Lorenz, *Z. Phys. Chem.*, 1914, **87U**, 513–542.
9 G. Cochrane and N. H. Fletcher, *J. Phys. Chem. Solids*, 1971, **32**, 2557–2567.
10 T. Takahashi, *J. Appl. Electrochem.*, 1973, **3**, 79–90.
11 K. Funke, *Prog. Solid. State Chem.*, 1976, **11**, 345–402.
12 S. Hull, *Rep. Prog. Phys.*, 2004, **67**, 1233–1314.
13 M. Tatsumisago, Y. Shinkuma and T. Minami, *Nature*, 1991, **354**, 217–218.
14 R. Makiura, T. Yonemura, T. Yamada, M. Yamauchi, R. Ikeda, H. Kitagawa, K. Kato and M. Takata, *Nat. Mater.*, 2009, **8**, 476–480.
15 S. Yamasaki, T. Yamada, H. Kobayashi and H. Kitagawa, *Chem. Asian J.*, 2013, **8**, 73–75.
16 T. Yamamoto, M. Maesato, N. Hirao, SI. Kawaguchi, S. Kawaguchi, Y. Ohishi, Y. Kubota, H. Kobayashi and H. Kitagawa, *J. Am. Chem. Soc.*, 2017, **139**, 1392–1395.
17 T. Yamamoto, H. Kobayashi, L. S. R. Kumara, O. Sakata, K. Nitta, T. Uruga and H. Kitagawa, *Nano Lett.*, 2017, **17**, 5273–5276.
18 J. Maier, *Prog. Solid. State Chem.*, 1995, **23**, 171–263.
19 K. L. Kliewer and J. S. Koehler, *Phys. Rev.*, 1965, **140**, A1226–A1240.
20 K. L. Kliewer, *Phys. Rev.*, 1965, **140**, A1241–A1246.
21 K. L. Kliewer, *J. Phys. Chem. Solids*, 1966, **27**, 705–717.
22 T. Jow and J. B. Wagner Jr, *J. Electrochem. Soc.*, 1979, **126**, 1963–1972.
23 R. C. Agrawal and R. K. Gupta, *J. Mater. Sci.*, 1999, **34**, 1131–1162.
24 C. C. Liang, *J. Electrochem. Soc.*, 1973, **120**, 1289–1292.
25 M. Nagai and T. Nishino, *J. Electrochem. Soc.*, 1991, **138**, L49–L51.
26 M. Nagai and T. Nishino, *Solid State Ionics*, 1992, **53–56**, 63–67.
27 M. Nagai and T. Nishino, *J. Am. Chem. Soc.*, 1993, **76**, 1057–1060.
28 M. Nagai and T. Nishino, *Solid State Ionics*, 1999, **117**, 317–321.
29 K. Tadagana, K. Imai, M. Tatsumisago and T. Minami, *J. Electrochem. Soc.*, 2000, **147**, 4061–4064.
30 H. Yamada, A. J. Bhattacharyya and J. Maier, *Adv. Funct. Mater.*, 2006, **16**, 525–530.
31 H. Yamada, I. Saruwatari, N. Kuwata and J. Kawamura, *J. Phys. Chem. C*, 2014, **118**, 23845–23852.
32 C. Liang, K. Terabe, T. Hasegawa and M. Aono, *J. Appl. Phys.*, 2007, **102**, 124308.
33 C. Liang, K. Terabe, T. Tsuruoka, M. Osada, T. Hasegawa and M. Aono, *Adv. Funct. Mater.*, 2007, **17**, 1466–1472.
34 H. Zhang, T. Tsuchiya, C. Liang and K. Terabe, *Nano Lett.*, 2015, **15**, 5161–5167.
35 L. Liu, S. Lee, J. Li, M. Alexe, G. Rao, W. Zhou, J. Lee, W. Lee and U. Gösele, *Nanotechnology*, 2008, **19**, 495706.
36 W. Lee, H. Yoo and J. Lee, *Chem. Commun.*, 2001, 18318–18322.
37 K. Tadagana, K. Imai, M. Tatsumisago and T. Minami, *J. Electrochem. Soc.*, 2002, **149**, A773–A777.
38 S. Albert, N. Frolet, P. Yot, A. Pradel and M. Ribes, *Solid State Ionics*, 2006, **177**, 3009–3013.
39 S. V. Baryshnikov, C. Tien, E. V. Charnaya, M. K. Lee, D. Michel, W. Böhlmann and N. P. Andriyanova, *Phys. Solid State*, 2008, **50**, 1342–1346.
40 S. V. Baryshnikov, C. Tien, E. V. Charnaya, M. K. Lee, D. Michel, W. Böhlmann and N. P. Andriyanova, *J. Phys.: Condens. Matter*, 2008, **20**, 025214.
41 A. Pradel, P. Yot, S. Albert, N. Frolet and M. Ribes, in *Nanostructured Materials for Advanced Technological Applications*, ed. J. P. Reithmaier, P. Petkov, W. Kulisch and C. Popov, Springer, Dordrecht, 2009, pp. 233–243.
42 P. G. Yot, S. Albert, N. Frolet, M. Ribes and A. Pradel, *J. Phys. Chem. C*, 2010, **114**, 18318–18322.
43 A. V. Il'inskii, R. A. Aliev, D. A. Kurdyukov, N. V. Sharenkova, E. B. Shadrin and V. G. Golubev, *Phys Status Solidi A*, 2006, **203**, 2073–2077.
44 M. Reháková, M. Casciola, I. G. K. Andersen and Z. Bastl, *J. Incl. Phenom. Mol. Recognit. Chem.*, 1996, **25**, 303–312.
45 L. D. Hart, *Alumina Chemicals: Science and Technology Handbook*, The American Ceramic Society, Ohio, 1990.
46 E. P. Barrett, L. G. Joyner and P. P. Halenda, *J. Am. Chem. Soc.*, 1951, **73**, 373–380.
47 R. D. Shannon, *Acta Crystallogr. A*, 1976, **32**, 751–767.
48 H. Maekawa, R. Tanaka, T. Sato, Y. Fujimaki and T. Yamamura, *Solid State Ionics*, 2004, **175**, 281–285.
49 H. Maekawa, Y. Fujimaki, H. Shen, J. Kawamura and T. Yamamura, *Solid State Ionics*, 2006, **177**, 2711–2714.
50 A. L. Bail, H. Duroy and J. L. Fourquet, *Mater. Res. Bull.*, 1988, **23**, 447–452.
51 J.-S. Lee, S. Adams and J. Maier, *J. Electrochem. Soc.*, 2000, **147**, 2407–2418.
52 M. Wasiucionek, K. Galazka, J. E. Garbarczyk, J. L. Nowinski, S. Gierlotka and B. Palosz, *Solid State Ionics*, 2011, **192**, 113–117.

53 J.-S. Lee, S. Adams and J. Maier, *Solid State Ionics*, 2000, **136–137**, 1261–1266.
54 Y.-G. Guo, J.-S. Lee and J. Maier, *Adv. Mater.*, 2005, **17**, 2815–2819.
55 Y.-G. Guo, J.-S. Lee, Y.-S. Hu and J. Maier, *J. Electrochem. Soc.*, 2007, **154**, K51–K60.
56 H. L. Tuller, *Solid State Ionics*, 2000, **131**, 143–157.
57 K. S. W. Sing, D. H. Everett, R. A. W. Haul, L. Moscou, R. A. Pierotti, J. Rouquerol and T. Siemieniewska, *Pure & Appl. Chem.*, 1985, **57**, 603–619.
58 A. Bunde and W. Dieterich, *J. Electroceram.*, 2000, **5**, 81–92.
59 N. F. Uvarov, P. Vaněk, M. Savinov, V. Železný, V. Studnička and J. Petzelt, *Solid State Ionics*, 2000, **127**, 253–267.
60 Y. Meng, J. Gao, Z. Zhao, J. Amoroso, J. Tong and K. S. Brinkman, *J. Mater. Sci.*, 2019, **54**, 9291–9312.